



1 Voxel inversion of airborne electromagnetic 2 data for improved groundwater model 3 construction and prediction accuracy

4 N. K. Christensen¹, and T.P.A Ferre², G. Fiandaca¹, S. Christensen¹

5 [1]{Department of Geoscience, Aarhus University, Aarhus,Denmark }

6 [2]{Department of Hydrology and Water Resources, University of Arizona, Tucson, USA. }

7 Correspondence to: N. K. Christensen (phda.nikolaj.kruse@geo.au.dk)

8 **Abstract**

9 We present a workflow for automated construction and calibration of large-scale groundwater models
10 that includes the integration of airborne electromagnetic (AEM) data and hydrological data. The AEM
11 data are inverted to form a 3D geophysical model. The parameter of interest is the hydraulic
12 conductivity, which can be determined by translating the 3D geophysical model, using a petrophysical
13 relationship, to form a 3D hydraulic conductivity distribution. We use the geophysical models and
14 hydrological data to determine the optimum spatially distributed petrophysical relationship. The two
15 shape factors of the petrophysical relationship primarily work as translators between resistivity and
16 hydraulic conductivity, but the shape factors can also compensate for structural defects in the model.

17 The method is demonstrated for a synthetic case study. The AEM data are inverted with both
18 smoothness (smooth) and minimum gradient support (sharp) constraints, resulting in two competitive
19 geophysical models. The value of the AEM data quality is tested by inverting the alternative
20 geophysical models using data corrupted with four different levels of background noise. Subsequently,
21 the geophysical models are used to construct two competing groundwater models. The performance of
22 the flow model was tested for four types of prediction. All predictions occurred beyond the calibration
23 base. Predictions of a pumping well's recharge area and groundwater age were applying the same
24 stress situation as applied during hydrologic model calibration, while predictions of head and stream
25 discharge was done for a stress situation changed from those applied during hydrologic model
26 calibration.

27 The results show that geophysical models inverted with sharp constraints improve the predictive
28 capability of the groundwater models compared to geophysical models inverted with smooth
29 constraints. It was found that the use of sharp models improves the prediction of recharge area, while



1 prediction of groundwater age does not improve significantly. When the stress situation is changed the
2 prediction of head change and stream discharge improves significantly for sharp models compared to
3 smooth models. This is especially true for predictions of head change made in the vicinity of the
4 pumping well and far-away from hydrologic boundaries. Furthermore, the geophysical data quality has
5 variable influence on different model predictions. Prediction accuracy improves with AEM data
6 quality for predictions of recharge area, head change and stream discharge, while the accuracy appears
7 to not improve for prediction of groundwater age.

8 **1 Introduction**

9 Large-scale geological and groundwater models are used extensively to support aquifer management.
10 (Here “large scale” refers to an area of from tens to thousands of square kilometers.) Determining the
11 distribution of hydraulic properties and the geometry and connectivity of the groundwater system is of
12 significant importance since these features control the flow paths (Desbarats and Srivastava 1991;
13 Fogg et al. 1999; Weissmann and Fogg 1999). Incorrect reconstruction of the geological structures has
14 thus been recognized as the most important source of uncertainty when a groundwater model is used to
15 make predictions outside its calibration base (Refsgaard et al. 2012; Seifert et al. 2012; Zhou et al.
16 2014). The data traditionally used for structural mapping include lithological logs from boreholes,
17 hydrological data, and hydraulic testing results, but these data are often sparse and uneven distributed
18 within an investigated domain. In these (very common) cases, data scarcity becomes a major obstacle
19 for structural mapping in relation to large scale groundwater modeling (Refsgaard et al. 2012; Zhou et
20 al. 2014).

21 Ground-based and airborne electromagnetic method (AEM) methods have shown a great potential for
22 mapping of geological structures (Jørgensen et al. 2003; Thomsen et al. 2004; Abraham et al. 2012;
23 Oldenborger et al. 2013; He et al. 2014; Munday et al. 2015). For large scale mapping AEM is an
24 efficient and cost-effective method by which the traditional data can be supplemented by dense
25 estimates of electrical resistivity which in some environments inform about the lithology and thereby
26 about structure (Robinson et al. 2008; Binley et al. 2015). The AEM measurements can quickly be
27 made over large areas, and the resolution can be as fine as 25 m in the horizontal direction and 5 m in
28 the vertical (Schamper et al. 2014) with penetration depth of up to several hundred meters (Siemon et
29 al. 2009).

30 Various methods have been reported for how to incorporate resistivity estimates (from now on called
31 resistivity models) in groundwater model construction. Manual and knowledge driven approaches
32 have been used to combine geological, hydrological and geophysical data with expert knowledge
33 (Jørgensen et al. 2013). However, the manual approach is subjective and possibly very time



1 consuming and expensive to use when resistivity models from large AEM surveys are to be
2 incorporated in model construction. Alternatively, more objective and cost-efficient geostatistical
3 modeling approaches (Carle and Fogg 1996; Deutsch and Journel 1998; Strebelle 2002) are available
4 for generating models from a combination of borehole information and AEM determined resistivity
5 models. For example: He et al. (2014) used a transition probability indicator simulation approach
6 (Carle and Fogg 1996), while Gunnink and Siemon (2015) used sequential indicator simulation
7 (Deutsch 2006). Marker et al. (2015) used a deterministic strategy for the integration of AEM
8 resistivity models into the hydrological modeling process.

9 The just mentioned studies all used sequential hydrogeophysical inversion approaches (SHI; as
10 defined by Ferré et al. 2009). In SHI the geophysical data are inverted first and independently from the
11 later inversion of the hydrological data. For large scale groundwater modeling Herckenrath et al.
12 (2013) and Christensen et al. (2016) were using both SHI and joint hydrogeophysical inversion
13 approaches (JHI; as defined by Ferré et al. 2009). By JHI the geophysical and hydrological data are
14 inverted jointly by linking the geophysical and hydrological models directly through some of their
15 parameters. The linking can for example be done by using an Archie's law inspired petrophysical
16 relationship (Archie 1942) to translate between the geophysical and hydrologic parameters.

17 In general, petrophysical relationships are difficult to establish, because such translation tend to be
18 site, scale and facies specific (Chen et al. 2001; Hyndman and Tronicke 2005; Slater 2007) and
19 uncertain (Mazáč et al. 1985; Slater 2007). The studies by Herckenrath et al. (2013) and Christensen
20 et al. (2016) were using a fixed petrophysical relationship throughout the model domain. Better results
21 can potentially be obtained by using a spatially variable relationship which allows for local translation
22 between hydraulic conductivity and electrical resistivity, and by including the spatially dependent
23 petrophysical parameters in the optimization process (Linde et al. 2006).

24 There are two other challenges for incorporating resistivity models into large scale groundwater
25 modeling: difference in model discretization, and choice of geophysical regularization methodology.
26 Groundwater models are often discretized in a regular voxel grid while the traditional resistivity
27 models are 1D and placed at the respective sounding location. For airborne surveys, for example, the
28 resistivity models are normally located along the flight lines (Christiansen et al. 2006). Such resistivity
29 models therefore need to be relocated to conform to the grid of the groundwater model. The relocation
30 will often be a subtle process where information easily can be lost. To accommodate this issue
31 Fiandaca et al. (2015) presented a geophysical modeling approach referred to as "voxel inversion"
32 which decouples the geophysical inversion model space from the geophysical measurement positions.
33 This allows estimation of a 3D geophysical model that is discretized on the same voxel grid as the
34 groundwater model.



1 Traditionally, geophysical regularization includes horizontal and vertical smoothing constrains
2 (Constable et al. 1987) or a few layer inversion (Auken and Christiansen 2004), whereas a
3 groundwater system often has sharp layer or body boundaries. It has therefore been recognized, e.g. by
4 Day-Lewis (2005) and others, that the regularization used to stabilize the geophysical inversion may
5 not reflect the actual hydrologic conditions unless it is chosen carefully. If, for example, smooth
6 regularization is used to estimate resistivity models in a sharply layered system it will produce a
7 blurred resistivity distribution from which one should be careful with inferring the spatial distribution
8 of hydraulic conductivity to be used in a groundwater model. In this case it would be better to use
9 minimum gradient support regularization (Portniaguine and Zhdanov 1999; Blaschek et al. 2008;
10 Vignoli et al. 2015) for the geophysical inversion because thus estimated resistivity distribution tend to
11 consist of fewer and more sharply defined layer boundaries (vertically and horizontally).

12 In this paper we present a sequential hydrogeophysical approach for using a voxel based 3D resistivity
13 model to parameterize and calibrate a groundwater model. We will demonstrate that the model
14 parameterization allows the calibration to compensate for errors in the resistivity model. We will also
15 demonstrate that it is important for groundwater modeling that the underlying resistivity model is
16 estimated by regularization constraints that conform well to the geological environment. Finally we
17 analyze how groundwater model prediction accuracy depends on the quality of the geophysical data
18 that was used to estimate the resistivity model. Section 2 of the paper presents the methodology.
19 Section 3 describes the synthetic test case used for our demonstration purposes. Section 4 presents the
20 results, while sections 5 and 6 discusses and draws the conclusions, respectively.

21

22



1 **2 Methodology**

2 Conceptually, the methodology defines a translator function that describes the petrophysical
3 relationship between electrical resistivity and hydraulic conductivity. A fundamental aspect is that the
4 petrophysical relationship can vary horizontally and vertically, thereby adapting to the local conditions
5 in translation from the geophysical model space to the hydrological model space. Through inversion,
6 the 3D spatially dependent optimal parameters of the petrophysical relationship are estimated for each
7 layer interval, thereby covering the entire three-dimensional model space.

8 Figure 1 provides a workflow for the method. First, the gathered airborne electromagnetic (AEM) data
9 from the survey area are inverted with smooth or sharp horizontal and vertical constraints (Vignoli et
10 al. 2015). This is done by using a recently developed voxel inversion scheme which decouples the
11 geophysical model from the position of the acquired data (Fiandaca et al. 2015). The geophysical
12 model space thus corresponds to the full 3D hydrological model grid. Secondly, the geophysical voxel
13 based resistivity model is used as input for the subsequential hydrological inversion. The geophysical
14 model parameter (resistivity) is linked to the main investigated parameter (hydraulic conductivity)
15 through a petrophysical relationship which has unknown shape factor values. The shape factor values
16 are estimated through a hydrological inversion which minimizes an objective function describing the
17 misfit between simulated groundwater model responses and corresponding observed hydrological
18 data. Finally, the calibrated groundwater model can be used to make a set of relevant hydrologic
19 predictions. The various steps of the methodology are explained in more detail in the following.

20

21 **2.1 Geophysical voxel inversion**

22 The AEM data undergoes constrained deterministic inversion (Figure 1, box 1) using a recently
23 developed voxel inversion approaches. This approach allows the geophysical model spaces to be
24 spatially decoupled from the geophysical measurement positions (Fiandaca et al. 2015). In most
25 inversion schemes the forward and inverse formulations use the same model discretization for both
26 inversion and forward calculation, but in the voxel formulation the two model discretizations are
27 decoupled. The voxel model space thus defines the geophysical properties on a set of nodes of a
28 regular 3D grid.

29 For calculating the forward responses, a “virtual” 1D model is a built at each sounding position. The
30 “virtual” 1D model is defined by a number of layers, and layer thicknesses. The geophysical properties
31 are interpolated from the voxel model space into the layer centers of the virtual model that is
32 subsequently used to simulate the forward response for the corresponding sounding.



1 The voxel inversion approach thus allows for inverting AEM data into a geophysical model defined on
 2 a 3D regular grid, regardless of the sounding positions. This implies that the geophysical inversion can
 3 be conducted using the same grid as that defined for a 3D groundwater model. Scaling issues in the
 4 coupling of geophysical and hydrological models can thus be avoided by using the same spatial
 5 discretization.

6 The general solution to the non-linear geophysical inversion problem can be found in Auken et al.
 7 (2014). To stabilize the inverse problem, either of two types of regularization methods can be applied.
 8 The first regularization method is commonly referred to as smoothness-constrained inversion
 9 (Constable et al. 1987). The smoothness-constrained inversion tends to reduce contrasts and the
 10 resulting geophysical model may appear blurred. The reason for this is found in its minimum-structure
 11 L2 norm inversion formalism (Constable et al. 1987; Menke 2012), which following the notation used
 12 by Vignoli et al. (2015) can be expressed as:

$$(m_i - m_j)^2 / \sigma_{i,j}^2 \quad (1)$$

13 where the m_i and m_j are the constrained parameters and $\sigma_{i,j}$ defines the constraint strength. The
 14 penalization of structures is clearly seen in eq. (1), where $(m_i - m_j)^2 / \sigma_{i,j}^2$ is proportional to the
 15 square of the value of the variation $(m_i - m_j)$. This implies that an increase in model parameter
 16 variation will always result in a penalization in the stabilizer. The smoothness regularization thus
 17 prevents reconstruction of sharp transitions.
 18

19
 20 The second regularization method is the minimum gradient support (Portniaguine and Zhdanov 1999;
 21 Blaschek et al. 2008; Vignoli et al. 2015), which allows for large sharp vertical and horizontal model
 22 transitions. The minimum gradient support regularization seeks to minimize the spatial variations
 23 vertically and laterally by penalizing the vertical and horizontal model gradients through the stabilizer
 24 expressed as (Vignoli et al., (2015)):

$$\frac{(m_i - m_j)^2 / \sigma_{i,j}^2}{(m_i - m_j)^2 / \sigma_{i,j}^2 + 1} \quad (2)$$

25



1 In eq. (2) $\sigma_{i,j}$ is a parameter used to control the sharpness of the regularization constraints. The
2 stabilizer contribution to the objective function is thus one when $|m_i - m_j| \gg \sigma_{i,j}$ and zero when
3 $\sigma_{i,j} \gg |m_i - m_j|$. The minimum gradient support functional thus counts the number of model
4 variations larger than $\sigma_{i,j}$ for the stabilizer term of the objective function. This formalism thus allows
5 sharp vertical and horizontal model transitions, which are excessively penalized by the smoothness-
6 constrained inversion.

7

8 **2.2 Hydrological model parametrization**

9 Section 2.1 describes an inversion methodology for which the geophysical property distribution can be
10 estimated for each element in a voxel grid (Figure 1, box 1). The three dimensional distribution of
11 electrical resistivity values is linked to the main investigated hydrological parameters (e.g. hydraulic
12 conductivity) through a petrophysical relationship.

13 Linking hydraulic conductivity and electrical resistivity is not trivial because the parameter values and
14 the form of the petrophysical relationship may vary dramatically between different types of
15 environments. In addition, there can be fundamental questions about how the effective properties
16 controlling electrical current flow are related to the effective properties controlling fluid flow (Slater
17 2007). The primary factors controlling this relationship are porosity, pore water conductivity,
18 tortuosity, grain size, degree of saturation, amount of clay minerals, etc. (McNeill 1980). The simplest
19 petrophysical relationship is the empirical relationship known as Archie's law (Archie 1942) that
20 relates porosity, pore water conductivity, and the degree of saturation to bulk electrical conductivity.
21 However, this type of relationship does not take the electrical surface conductance on the surface of
22 clay minerals into account. The Waxman and Smith model (Waxman and Smits 1968) combined with
23 the dual-water model by Clavier et al. (1984) provides a basis for establishing empirical relationships
24 for shaly sand and sediments containing clays (Revil and Cathles 1999; Revil et al. 2012). For glacial
25 sedimentary environments, it is reported that clay has low electrical resistivity and also low hydraulic
26 conductivity, and sand has high electrical resistivity and high hydraulic conductivity (Mazáč et al.
27 1985). It is common to use a power law relationship which is given some theoretical support by
28 Purvance and Andricevic (2000). The relationship is expressed as

$$K = \alpha \cdot \rho^\beta \quad (3)$$

29

30 where K is the hydraulic conductivity (m/s), ρ is the electrical resistivity (ohm-m), and α and β are
31 two empirical shape factors. To compute K for each element in the groundwater model grid, α and β



1 need to be parameterized and estimated. We suggest to make the parameterization by pilot points
 2 placed in a regular grid in each layer of the groundwater model (Certes and De Marsily 1991; Doherty
 3 2003). Each pilot point holds a set of α and β parameters, and kriging is used for spatial interpolation
 4 of α and β from the pilot points to the model grid. This kind of parametrization creates smooth
 5 transitions in the parameter fields and allows for variation in both the horizontal and vertical direction
 6 of the ρ to K translation. Hydraulic conductivity can thus be calculated by eq. (3) for every element
 7 in the groundwater model grid.

8

9 **2.3 Hydrological Inversion**

10 The model parameters, α and β at the pilot points, are calibrated by fitting the groundwater model to
 11 hydrological data. When the number of model parameters is large compared to the number of
 12 observation data, the minimization must be stabilized by regularization. The total objective function
 13 to be minimized is therefore a balanced compromise between a measurement term (Φ_m) and a
 14 regularization term (Φ_r). The combined objective function has the form

$$\Phi_{total} = \Phi_m + \mu \cdot \Phi_r = \sum_{i=1}^{n_d} \omega_{d,i} (d_{obs,i} - d_{sim,i})^2 + \mu \cdot \Phi_r \quad (4)$$

15

16 where Φ_{total} is the total objective function, $d_{obs,i}$ and $d_{sim,i}$ are measured and equivalent simulated
 17 data values, $\omega_{d,i}$ is a data dependent weight, μ is a weight factor, and ϕ_r is a Tikhonov regularization
 18 term. Here, ϕ_r is defined as preferred difference regularization, where the preferred difference
 19 between neighboring parameter values is set to zero. Φ_{total} is minimized iteratively, and the
 20 regularization weight factor, μ , is calculated during the iteration in a way so Φ_m , the measurement part
 21 of the objective function, becomes approximately equal to a user specified target value (Doherty
 22 2010).

23

24 **3 Synthetic example**

25 For illustrative purposes we use a three dimensional synthetic system very similar to that presented by
 26 Christensen et al. (2015). The only difference is that the active part of the groundwater system only
 27 consists of 5 layers whereas Christensen et al. (2015) used a 20 layer model.



1 **3.1 Groundwater reference system and hydrological data**

2 The groundwater system is intended to mimic a glacial landscape and covers an area that is 7000 m
3 (N-S) by 5000 m (E-W). The geology of the system was generated using T-PROGS (Carle 1999) as
4 having a horizontal discretization of 25 m x 25 m, and a vertical discretization of 10 m. The system
5 extends 50 m in the vertical direction where it reaches impermeable clay with a horizontal surface.
6 The T-PROGS generated geology above the impermeable clay consists of categorical deposits of sand,
7 silt and clay. Within each of the three types of deposits, hydraulic conductivity, recharge and the
8 porosity were generated as horizontally correlated random fields using FIELDGEN (Doherty 2010).
9 All boundaries of the domain were defined as having no-flow conditions except the southern boundary
10 where hydraulic head was defined as constant, $h = 0$ m. The local recharge depends on the type of
11 sediment at the uppermost layer. Most groundwater discharges through the southern boundary, but
12 approximately 35% discharges into a river running north to south in the middle of the domain (Figure
13 2). Groundwater flow was simulated as confined steady-state flow employing MODFLOW-2000
14 (Harbaugh et al. 2000) with the spatial discretization equal to the geological discretization.
15 Groundwater is pumped at a rate of $0.015 \text{ m}^3\text{s}^{-1}$ from a well located at $x=2487.5\text{m}$ and $y=1912.5\text{m}$ and
16 the well screens the deepest 10 meters of the groundwater system. In the following this system is
17 called the *reference system*.

18 Thirty-five boreholes are found within the domain (Figure 2). Each borehole contains a monitoring
19 well that screens the deepest 10 m of sand registered in the borehole. For each system realization,
20 hydraulic head in the 35 wells and the river discharge at the southern boundary were extracted from a
21 forward simulation made by MODFLOW-2000. The 35 simulated hydraulic head values were
22 contaminated by independent Gaussian error with zero mean and 0.1 m standard deviation. The river
23 discharge was corrupted with independent Gaussian error with zero mean and a standard deviation
24 corresponding to 10 % of the true river discharge. The 36 contaminated values constitute the
25 hydrological data used for groundwater model calibration.

26

27 **3.2 Geophysical reference system and data**

28 The geophysical reference system was designed so there is perfect correlation between hydraulic
29 conductivity and electrical resistivity. This implies that a relationship between hydraulic conductivity
30 and measured electrical resistivity is likely to exist. The true relationship is of the same form as eq. (3
31), and it uses constant shape factor values $\alpha = 1e^{-12}$ and $\beta = 4$. This corresponds to conditions
32 where clay has low electrical resistivity and also low hydraulic conductivity, and sand has high



1 electrical resistivity and high hydraulic conductivity. The impermeable clay at the base of the
2 reference system was assigned a constant value of 5 ohm-m.

3 The AEM data were simulated using AarhusInv (Auken et al. 2014) for a system setup similar to a
4 typical dual-moment SkyTEM-304 system (Sørensen and Auken 2004). The simulated survey consists
5 of 35 E-W flight lines with 200 meter spacing between the flight lines. AEM system responses were
6 simulated for every 25 m along the flight lines giving a total of 6300 sounding locations for both the
7 transmitted high and low moments. AarhusInv is a 1D modeling code. To mimic the loss of resolution
8 with layer depth we simulated the responses using the 2D logarithmic average resistivity of all model
9 cells inside the radius of the foot print at a given depth.. To obtain the geophysical data set, the
10 simulated data were contaminated with noise according to the noise model suggested by (Auken et al.
11 2008):

$$V_{resp} = V \cdot \left(1 + G(0,1) \cdot \left[STD_{uni}^2 + \left(\frac{V_{noise}}{V} \right)^2 \right]^{1/2} \right) \quad (5)$$

12

13 where V_{resp} is the perturbed synthetic data, V is the synthetic noiseless data, $G(0,1)$ is standard
14 Gaussian noise (with zero mean and unit standard deviation), and STD_{uni}^2 is uniform noise variance.
15 V_{noise} is the background noise contribution given by

$$V_{noise} = b \cdot \left(\frac{t}{10^{-3}} \right)^{-1/2}, \quad (6)$$

16

17 where t is the gate center time in seconds, and b is the background noise level at 1 ms. For the
18 following analysis we generated geophysical datasets with four levels of background noise, i.e. b equal
19 to 1, 3, 5, and 10 nV/m², respectively. The uniform standard deviation, which accounts for instrument
20 and other non-specified noise contributions, was set to 3% for dB/dt responses. After the data were
21 perturbed with noise, it was processed as a field data set (Auken et al. 2009), resulting in an uneven
22 number of gates per sounding. Figure 3 illustrates the resulting low and high moment AEM sounding
23 data, respectively, for the different background noise levels.

24



1 **3.3 Geophysical voxel inversion**

2 The geophysical data were inverted by voxel inversion (Fiandaca et al. 2015) using AarhusInv (Auken
3 et al. 2014). The voxel inversion was conducted in two different ways: by using L2-norm “smooth”
4 constraints, or by using minimum gradient support “sharp” constraints (both implemented in
5 AarhusInv; Auken et al. 2014).

6 To avoid the influence of numerical discretization errors, the geophysical voxel inversion uses the
7 same spatial discretization as the reference system and the groundwater model. For both smooth and
8 sharp inversions a 40 ohm-m uniform half-space was used as starting model, and spatial regularization
9 was applied using the same settings throughout all inversions. It was unnecessary to apply vertical
10 constraints for any of the inversions. (On the contrary, depth and direction dependent horizontal
11 constraint factors were used for both smooth and sharp inversions. For smooth regularization
12 constraint factors of 1.9 along the flight lines and 1.05 perpendicular to the flight lines was used for
13 the first layer. The constraint factors was set to decrease linear with depth, resulting in constraint
14 factors of 1.4 along the flight lines and 1.02 perpendicular to the flight lines for the sixth layer. For
15 sharp inversion, constraint factors of 1.0625 along the flight lines and 1.01 perpendicular to the flight
16 lines was used for the first layer, while factors of 1.025 along the flight lines and 1.01 perpendicular to
17 the flight lines was used for the sixth layer.

18 **3.4 Groundwater model parametrization and calibration**

19 In the following the groundwater model will be parameterized in two different ways. Both ways treat
20 the shape factors α and β of the relationship (3) between hydraulic conductivity and resistivity as
21 spatially dependent parameters to be estimated. The two parameterizations differ by the resistivity
22 model that is used to calculate the hydraulic conductivity field of the groundwater model:

- 23 • The first type of parameterization uses a resistivity model estimated by smooth voxel inversion of
24 AEM data collected with a background noise level of 3 nV/m². These models will be referred to
25 as SHI-smooth-3.
- 26 • The second type of parameterization uses a resistivity model estimated by sharp voxel inversion of
27 AEM data collected with a background noise level of either 1, 3, 5, or 10 nV/m². These models
28 will be referred to as SHI-sharp-1, SHI-sharp-3, SHI-sharp-5, and SHI-sharp-10, respectively.

29 The shape factors α and β of the petrophysical relationship are parametrized by placing pilot points in
30 a uniform grid, with 5 nodes in the x direction and 7 in the y direction. Hence, in total the groundwater
31 model is parameterized by $5 \times 7 \times 5 = 175$ petrophysical relationships each having two parameters (the
32 shape factors).



1 The parameter values are estimated by fitting the available hydrological data consisting of the 35
 2 observations of hydraulic head and one river discharge observation. Calibration is done by
 3 minimization the total objective function given by eq. (4), where the measurement objective function
 4 is computed as

$$\Phi_m = n_h^{-1} \sum_{i=1}^{n_h} \omega_h (h_{obs,i} - h_{sim,i})^2 + n_r^{-1} \sum_{i=1}^{n_r} \omega_r (r_{obs,i} - r_{sim,i})^2 \quad (7)$$

5
 6 where, n_h and n_r are the number of head and river measurements, respectively; h_{obs} and h_{sim} are
 7 observed and corresponding simulated hydraulic heads; r_{obs} and r_{sim} are observed and
 8 corresponding simulated river discharge; and ω_h and ω_r are subjectively chosen weights for head and
 9 discharge data, respectively. We strived at choosing values of ω_h and ω_r that give an average value
 10 of $\bar{\phi}_m = 2$, where the average is calculated over the 20 system realizations. Such values of ω_h and ω_r
 11 will then be estimates of the reciprocal of the total error variance for hydraulic head and discharge,
 12 respectively. This is seen from (7). By trial and error we found $\omega_h = 1$ and $\omega_r = 1.38 \cdot 10^5$ which
 13 gave $\bar{\phi}_m = 2.5$. The value $\omega_h = 1$ corresponds to $(10 \cdot \sigma_h)^{-2}$ where σ_h is the standard deviation for
 14 the head measurements. The value $\omega_r = 1.38 \cdot 10^5$ corresponds to $(\sigma_r)^{-2}$, where σ_r is the standard
 15 deviation of the measurement error for measured discharge. These values thus indicate that the
 16 calibrated models have error in their simulation of hydraulic head but not in simulation of river
 17 discharge.

18

19 Calibration was performed using local search as optimization implemented in the parameter estimation
 20 software BeoPEST, a version of PEST (Doherty 2010) that allows the inversion to run in parallel
 21 using multiple cores and computers.

22 It should be noted that for calibration and model prediction we applied the recharge field and boundary
 23 conditions of the reference system.

24 3.5 Reference and model predictions

25 The calibrated SHI-smooth and SHI-sharp groundwater models are evaluated by comparing their
 26 simulated model predictions with corresponding predictions simulated for the reference system. The
 27 former are called “model predictions, the latter are called “reference predictions”.

28 Prediction types 1 and 2 relate to steady-state flow when groundwater is pumped from the well. This is
 29 also the condition for which the hydrologic data used for calibration were sampled. Type 1 is the



1 average age of the groundwater pumped from the well. Type 2 is the size of the recharge area of the
 2 pumping well. Both these predictions differ in type from the calibration data. For these model
 3 predictions we used a homogeneous porosity of 0.2 (the average value of the reference system porosity
 4 fields is 0.184).

5 Prediction types 3 and 4 relate to a new stress situation long after pumping from the well has ceased:
 6 type 3 is groundwater discharge into the stream, and type 4 is head recovery for a well screening layer
 7 north-east of the pumping well (location is shown in Figure 2).

8 The reference and model prediction types 3 and 4 were simulated by MODFLOW-2000 (Harbaugh et
 9 al. 2000), while type 1 and 2 were simulated by forward particle tracking using MODPATH version 5
 10 (Pollock 1994) and MODFLOW-2000 results.

11 The first two types of prediction are interesting from the perspectives of protection and resource-
 12 management of a well field, while the latter two are relevant in the case of possible change of
 13 management practice resulting in a new stress.

14

15 **3.6 Evaluation of prediction performance**

16 As said in the beginning of section 2, steps 1-3 of the framework can be repeated for a number of
 17 system realizations for making consistent statistical interference on the model prediction results. Here
 18 20 different reference system realizations were used. For each prediction we hereby have 20
 19 corresponding sets of reference predictions and model predictions that can be used to evaluate the
 20 performance of a calibrated model with respect to that prediction. The performance is evaluated for
 21 SHI-smooth and SHI-sharp models, respectively, and it is done in the following ways.

22 Prediction error characteristics are quantified by the mean absolute error (*MAE*), the mean error (*ME*),
 23 respectively:

24

$$MAE = \frac{1}{N} \sum_{i=1}^N |x_i - t_i| \quad (8)$$

$$ME = \frac{1}{N} \sum_{i=1}^N x_i - t_i \quad (9)$$

25



1 where x_i is the model prediction of realization i , t_i is the reference prediction of realization i , and
2 $N = 20$ is the number of system realizations. MAE measures how close the model prediction tends to
3 be to the reference prediction; ME measures the tendency of positive or negative bias in the model
4 prediction.

5

6 **4 Results**

7 **4.1 Geophysical results**

8 Figure 4 shows a representative cross-section for one of the 20 system realizations. Both geophysical
9 models in Figure 4 were inverted using data perturbed with a background noise level of 3nV/m^2 .
10 Comparing the geophysical model results with the reference model, we find that the SHI-smooth-3
11 resolves the main features reasonably well for the upper layers. The main discrepancy is found in the
12 fifth layer where the sand bodies are not resolved. In general, the resistivity of the sand bodies (dark
13 orange in the reference system) is underestimated and the transitions between the categorical deposits
14 are artificially smooth.

15 Figure 4 shows that SHI-sharp-3 resolves the sand body in layer 5 much better than SHI-smooth-3.
16 Moreover, the locations and boundaries of the geological deposits tend to be less smeared out when
17 using the sharp constraints. Inspection of the histograms at the bottom of Figure 4 shows that the SHI-
18 sharp-3 model tends to produce resistivity distributions that have more similarities with the reference
19 distributions than the SHI-smooth-3 model. This improvement should potentially allow for easier
20 translation from electrical resistivity into hydraulic conductivity and more faithful representation of
21 hydrogeologic structure and connectivity.

22 Figure 5 shows corresponding voxel by voxel density plots of reference versus estimated electrical
23 resistivity for a SHI-smooth model and corresponding SHI-sharp models. Pearson's correlation
24 coefficient (PCC; Cooley and Naff 1990) is shown on top of the density plot for each layer. A
25 comparison of the density plots and the PCC values of the SHI-smooth-3 and SHI-sharp-3 models
26 shows that using sharp instead of smooth constraints improves the inverted geophysical model. The
27 improvement is most clearly seen for the sand deposits

28 For both SHI-smooth and SHI-sharp models there is a strong correlation between the electrical
29 resistivity estimates and the true electrical resistivities of the first layer, but the SHI-smooth model has
30 weaker correlation than the SHI-sharp models. For both type of models the correlation weakens with
31 depth and background noise. The former is caused by the resolution limitations of AEM data.



1 However, the depth and resistivity of the low-resistivity clay at the base of the model are well resolved
2 by both the SHI-smooth and SHI-sharp models inversions (results not shown).

3 **4.2 Hydrological calibration results**

4 The calibration results for the 20 different system realizations are shown in Figure 6. The figure shows
5 the measurement objective function value, Φ_m , for each system realization. We aimed at using
6 weights that would make the minimized measurement objective function value averaged over the 20
7 system realizations approximately equal to 2. Figure 6 shows that this is nearly satisfied by the SHI-
8 Sharp models even for large background noise levels. For many of the realizations the SHI-Smooth
9 model also fits the data well, but for a couple of realizations the misfit is much larger than aimed at.
10 This makes $E[\Phi_m]$ equal to 5.8 for SHI-Smooth-3 models while it is 2.5 for the SHI-Sharp-3 models.
11 This indicates that the estimated hydraulic conductivity field tends to be less wrong for sharp models
12 than for smooth models.

13

14 **4.3 Parameter estimation**

15 Figure 7 shows a cross section of the estimated K -, α - and β - fields for one of the system realizations .
16 The two columns show estimates for the SHI-smooth-3 and SHI-sharp-3 models, respectively. Figure
17 8 shows a density plot of the reference hydraulic conductivity distribution and the estimated hydraulic
18 conductivity distributions. The results in Figure 7 and Figure 8 are typical for all 20 system
19 realizations.

20

21 From Figure 7 a) and Figure 7 b) it is seen that the estimated α and β parameter values are changing
22 smoothly in the horizontal direction but have sharp transitions in the vertical direction. The second
23 row of Figure 7 shows the corresponding estimated K fields whose main features are determined by
24 the underlying resistivity models (Figure 4), but they are “corrected” during model calibration to make
25 the groundwater fit the hydrological data.

26

27 For the SHI-smooth-3 model, α and β are taking compensatory roles particularly in the first layer.
28 Here the estimated α and β values in this layer are higher than the shape factors of the true
29 relationship that was used to construct the geophysical reference system. This increases the hydraulic
30 conductivity in layer 1 to compensate for the too low hydraulic conductivity (and resistivity, Figure 4)
31 in layer 2 and deeper layers. The estimated α and β values are not sufficient to compensate for the
32 missing deep high-resistivity body in in layer 5 of the SHI-Smooth-3 model (Figure 4).

33



1 For the SHI-sharp-3 model, the estimated α and β parameter values only vary slightly from the shape
2 factor values of the true relationship except for layer 5 (Figure 7 b)). This indicates that for the more
3 shallow layers the sharp inversion of AEM data sufficiently resolves the resistivity of features that are
4 important for groundwater model calibration. In layer 5 the estimate of shape factor β turns out to be
5 fairly high, this compensates for the too low resistivity estimates in this layer (Figure 4).

6 Figure 8 shows voxel by voxel density plots of reference versus estimated hydraulic conductivity for
7 SHI-smooth and SHI-sharp models. The figure is equivalent to Figure 5. Figure 8 confirms that the
8 resulting K field tends to be overestimated for the first layer, and in particular for the SHI-smooth-3
9 model. From the second layer and down the hydraulic conductivity values tend to be underestimated
10 for sand but overestimated for silt and clay. Moreover, the distributions of estimated K smear out with
11 depth. Judged by PCC values and visual inspection of Figure 8, the hydraulic conductivity field
12 estimated for SHI-sharp models is in better agreement with the reference field than the field estimated
13 by the SHI-Smooth-3 model.

14 Model structural accuracy is quantified in Table 1 for both the SHI-smooth and SHI-sharp models.
15 Structural accuracy is here calculated as the fraction of total number of voxels for which the estimated
16 \log_{10} -hydraulic conductivity plus/minus twenty percent contains the true \log_{10} -hydraulic conductivity
17 value of the reference model. The results are averaged over the 20 system realizations. From Table 1 it
18 is seen that all SHI-sharp models outperform the accuracy of the SHI-smooth models except for layer
19 5. The exception occurs because the SHI-smooth models are fairly good at estimating the K
20 distributions for silt and clays, but underestimates K for sand (Figure 8). On the contrary, SHI-models
21 overestimate the K distributions for silt and clays, but only slightly underestimate K for sand (Figure
22 8). Therefore, for layer 5 the model structural accuracy appears to be better for SHI-smooth than for
23 SHI-sharp models.

24

25 **4.4 Prediction results**

26 For each of the 20 system realizations, the calibrated groundwater models were used to make the
27 model predictions described in section 3.5. Figure 9 shows scatter plots of reference prediction versus
28 the calibrated model prediction; each plotted point corresponds to a particular system realization and
29 corresponding SHI-smooth-3 or SHI-sharp-3 model. The mean error (ME) and mean absolute error
30 (MAE) of the prediction are also given in Figure 9. Figure 10 shows a MAE contour map for head
31 recovery predictions.

32



1 4.4.1 Particle tracking predictions

2 The first column of Figure 9 shows results for prediction of average age of the groundwater pumped
3 from the pumping well. The scatter plot illustrates that SHI-sharp models tend to over-predict average
4 age. This is seen by the majority of points plotting above the identity line as well as by the value of
5 $ME = 32$ (Figure 9). The age prediction results are similar for the SHI-smooth models although the
6 spread of points is larger than for SHI-sharp-3 (e.g. quantified by the larger value of MAE). There are
7 two major explanations for these relatively “poor” predictive performances. First, the calibrated K-
8 fields underestimate hydraulic conductivity of sand deposits in the deeper layers (Figure 8), which
9 results in too slow particle travel times at depth. Secondly, the reconstruction of the deepest layers is
10 too smooth for both SHI-smooth and SHI-sharp models (Figure 7) and does not resolve the small-scale
11 variability that controls the transport of particles.

12 The second column of Figure 9 is for prediction of the recharge area of the pumping well. The scatter
13 plot shows that the SHI-smooth models under-predicts the recharge area. This happens because the
14 smooth models lead to estimation of hydraulic conductivities in the deepest layers that are too low.
15 This creates a deep cone of depression around the pumping well that extends upward locally to reach
16 the river bed. This induces a local discharge of water from the stream through the groundwater system
17 to the pumping well. These models thus predict that a significant proportion of the pumping comes
18 from local discharge from the river. (This is compensated by increased model predicted groundwater
19 discharge to other parts of the river.) For the corresponding reference systems, the river is not losing
20 water, and all water pumped from the well originates from groundwater recharge.

21 The SHI-sharp models are better predictors of the recharge area, but also these models tend to predict
22 an area too small. These models also predict local discharge from the river to the groundwater system,
23 but to a lesser degree than the SHI-smooth models. This is likely because the main features of the
24 reference system are better reconstructed by the SHI-sharp-3 models.

25

26 4.4.2 Head recovery and discharge predictions

27 The prediction of head recovery at the observation well is done poorly by the SHI-smooth-3 (Figure
28 9). The predicted head recovery is very small for most of these models because they tend to have too
29 little hydraulic connectivity between the deepest layers, the estimated hydraulic conductivities are too
30 low in the deep sand layers, and the simulated cone of depression is therefore too deep and too local.

31 The SHI-sharp-3 models make less biased, fairly reasonable predictions of the head recovery (Figure
32 9) because they resolve the variations of hydraulic conductivity at depth better than the SHI-smooth-3
33 models. The superiority of SHI-smooth-3 models for recovery prediction is also seen from the MAE



1 contour maps in Figure 9. The *MAE* is seen to be spatially dependent: it is largest at the pumping well,
2 and smallest at the constant head boundary to the south

3 The fourth column of Figure 9 shows that both types of models are good predictors of discharge to the
4 river after cessation of pumping. However, the SHI-sharp-3 model prediction is superior since its
5 points tend to plot close to the identity line. For SHI-smooth-3, the prediction tends to be positively
6 biased and more spread than for SHI-sharp-3.

7

8 **4.4.3 Prediction error as function of data quality**

9 In Figure 11 *MAE* is used as a metric to evaluate how the prediction performance of SHI-sharp
10 models depends on the level of background noise for the geophysical data. The noise levels were kept
11 unchanged for the hydrological data.

12 Figure 11 shows that the average age prediction made by SHI-sharp models are nearly unaffected by
13 the quality of the geophysical data. It is speculative, but this result may be because this prediction is
14 highly dependable on small scale variability in hydraulic conductivity and porosity that cannot be
15 resolved from any of the geophysical data sets.

16 It is different for the recharge area prediction (Figure 11): *MAE* increases for this by approximately
17 25% when the level of background noise is increased from 1 nV/m² to 10 nV/m². This happens
18 because the variations of resistivity (and thus hydraulic conductivity) are less well resolved from the
19 geophysical data of poor quality.

20 The third and fourth row of Figure 11 shows the head recovery and river discharge prediction after
21 cessation of the pumping well. Head recovery and discharge predictions also tend to depend on the
22 quality of the geophysical data. The *MAE* increases by 17 % for recovery prediction and 23 % for
23 discharge prediction when the noise level of the geophysical data increases from 1 nV/m² to 10 nV/m².

24



1 **5 Discussion**

2 **5.1 Estimation of Parameters in the Petrophysical Relation**

3 Parameterizing the groundwater model by assuming a spatially dependent petrophysical relationship
4 between resistivity and hydraulic conductivity makes it possible to use a resistivity voxel model for
5 construction and calibration of a groundwater model. By assuming the relationship to be spatially
6 dependent can account for two challenges: i) there may be actual changes in the petrophysical
7 relationship within an investigated domain, and ii) there may be resolution limitations in the estimated
8 resistivity model.

9 Challenge i) can for example be expected for sedimentary environments, where the formation
10 resistivity is primarily controlled by the pore water resistivity and the clay content. In the case of
11 spatially changes of pore water resistivity and/or content of various clay minerals content the
12 discrimination between clay and sands may be less clear in the estimated resistivity values. For large-
13 scale groundwater system the variation of pore water resistivity (e.g. saline pore water) is expected to
14 vary smoothly, which would be accounted for by the spatially varying petrophysical relationship.
15 However, the procedure only works if the underlying assumption that clay rich deposits have lower
16 electrical resistivity compared to sands deposits is valid.

17 Challenge ii) concerns the geophysical model resolution of the true formation resistivity. EM methods
18 are, by nature, more sensitive to deposits of low electrical resistivity than to deposits of high
19 resistivity, and their vertical and horizontal resolution decrease with depth. This challenge is what
20 affects the resistivity models estimated in the present synthetic study. Estimating spatially dependent
21 shape factors by groundwater model calibration let them take a compensatory role for the resolution
22 issues of the estimated geophysical voxel model. The calibrated shape factors may no longer have firm
23 physical meaning since they mainly act as correction parameters for absorbing structural errors of the
24 geophysical model. The estimation of locally unreasonable shape factors may be acceptable as long as
25 the resulting hydraulic conductivity values are reasonable. The idea of calibrating the shape factors is
26 related to the concept of compensatory parameters in highly parameterized calibration described by
27 Doherty and Welter (2010) and by Doherty and Christensen (2011).

28 Finally, Auken et al. (2008) showed that using borehole data as a priori information in the geophysical
29 inversion improves the reconstruction of the model features significantly. Estimation of EM-based
30 resistivity models should therefore in general be supported by borehole information to improve the
31 decreasing spatial resolution of the EM methods.

32



1 5.2 Geophysical inversion strategy and Data quality

2 Inversion of AEM data using a 1D geophysical model usually applies smoothness constraints in order
3 to regularize the inversion (Auken and Christiansen 2004; Viezzoli et al. 2008). Traditionally, the
4 regularization includes both lateral and vertical smoothing constraints (Constable et al. 1987) or a few
5 layer parametrization (Auken et al. 2008). Inversion using the former type of regularization produces
6 smooth images with blurred formation boundaries which can be problematic when it is important to
7 resolve structural connections in a complex geological system. The latter few-layer inversion may is
8 also be prone to produce artifacts when used to map complex geological environments. It has therefore
9 been recognized, e.g. by Day-Lewis (2005) and others, that the regularization used to stabilize the
10 geophysical inversion may lead to artifacts that do not reflect the actual hydrogeological conditions.
11 Thoughtless use of such results to construct groundwater models for making hydrologic predictions
12 can therefore have serious ramifications.

13

14 Furthermore, for the present case study, the number of vertical transitions is a great challenge for the
15 AEM method due to the principle of high resistivity equivalence: that is, it is difficult to resolve a
16 high-resistivity layer between two low-resistivity layers because the energy loss, and therefore the
17 sensitivity is concentrated in the more resistive layers. This will result in layer suppression, because
18 the data sensitivity to the high resistive layer is low (Christiansen et al. 2006). This effect is present for
19 both the smooth and sharp inversion, but in the sharp inversion the effect is less fuzzy and features,
20 especially for the fifth layer, are more clearly reconstructed (Figure 4). When the sensitivity of the
21 AEM method is too low, the contribution from the regularization may dominate, and information
22 might migrate from areas with higher measurement sensitivity (Vignoli et al. 2015). In contrast to the
23 smooth regularization scheme, the sharp regularization method is designed to penalize smooth
24 transitions, which eventually improves the reconstruction of the deeper sand bodies. Therefore, for the
25 present case study the sharp regularization methodology should be preferred over smooth
26 regularization, because sharp constraints correspond better to the true structures of the reference
27 system (categorical deposits with sharp transitions; Figure 4). Moreover, because the sharp
28 regularization methodology leads to improved reconstruction of subsurface structures, these models
29 lead to greater accuracy and improvement of most groundwater model predictions (Figure 9).

30

31 The groundwater system considered here is relatively shallow, at least seen from the perspective of the
32 AEM system used in the demonstration example. This is evident from the transmitted EM signal
33 (Figure 3). The background noise is primarily affecting the last time-gates (10^{-4} - 10^{-3} s) of the low-
34 moment and only to a small degree the high moment time gates (even for low quality data). This
35 implies that the resolution of the AEM data is generally high for the upper layers. Therefore, in the



1 present case the upper layers of all the geophysical models (both SHI-smooth and SHI-sharp) are well-
2 resolved and to a large extent unaffected by AEM data quality (Figure 5). However, the deep sand
3 units are difficult to resolve because they give only a weak signature in the AEM data (Figure 3,
4 Figure 5). This is particularly true for the poorest AEM data quality cases where the late time gates for
5 the low moment measurements are disturbed by background noise.

6 **6 Summary and Conclusion**

7 We present a workflow for automated construction and calibration of large-scale groundwater models
8 using a combination of airborne electromagnetic (AEM) data and hydrological data, but other types of
9 data could be integrated as well. First the AEM data are inverted to form a 3D geophysical model.
10 Subsequently, the geophysical model is translated to a 3D model of hydraulic conductivity by using a
11 spatially dependent petrophysical relationship for which the shape parameters are estimated by fitting
12 the groundwater model to hydrological data. The estimated shape factors of the petrophysical
13 relationship primarily work as translators between resistivity and hydraulic conductivity, but they can
14 also compensate for structural defects in the model.

15 The method is demonstrated for a synthetic case study where the subsurface consists of categorical
16 deposits with different geophysical and hydraulic properties. The AEM data are inverted using both
17 smooth and sharp regularization constraints, resulting in two competitive geophysical models.
18 Furthermore, the influence of the AEM data quality is tested by inverting the sharp geophysical
19 models using data corrupted with four different levels of background noise. The resulting groundwater
20 models are each calibrated on basis of head and discharge data, and their predictive performance is
21 tested for four types of prediction beyond the calibration base. Predictions of a pumping well's
22 recharge area and groundwater age are applying the same stress situation as applied during hydrologic
23 model calibration, while predictions of head and stream discharge is done for a changed stress
24 situation.

25 It is found that a geophysical model inverted with sharp constraints (SHI-sharp) leads to a more
26 accurate groundwater model than one that is based on a geophysical model inverted with smooth
27 constraints (SHI-smooth). The SHI-sharp model leads to an estimated hydraulic conductivity field of
28 greater accuracy and to improvement of most groundwater model predictions. The explanation is that
29 the reference system (like many real hydrogeologic systems) is characterized by sharp transitions
30 between the categorical deposits; this is resolved better by the SHI-sharp model than by the SHI-
31 smooth model.



- 1 Finally, it is shown that prediction accuracy improves with AEM data quality for predictions of
- 2 recharge area, head change and stream discharge, while the accuracy appears to not improve for
- 3 prediction of groundwater age.



1 7 References

- 2 Abraham JD, Cannia JC, Bedrosian PA, Johnson MR, Ball LB, Sibray SS (2012) : Airborne
3 Electromagnetic Mapping of the Base of Aquifer in Areas of Western Nebraska. In: U.S. Geol.
4 Surv. Sci. Investig. Rep. 2011–5219. <http://pubs.usgs.gov/sir/2011/5219/>. Accessed 4 Jan 2016
- 5 Archie GE (1942) : The Electrical Resistivity Log as an Aid in Determining Some Reservoir
6 Characteristics. *Trans AIME* 146:54–62. doi: 10.2118/942054-G
- 7 Auken E, Christiansen A V., Jacobsen LH, Sørensen KI (2008) : A resolution study of buried valleys
8 using laterally constrained inversion of TEM data. *J Appl Geophys* 65:10–20.
- 9 Auken E, Christiansen AV (2004) : Layered and laterally constrained 2D inversion of resistivity data.
10 *GEOPHYSICS* 69:752–761. doi: 10.1190/1.1759461
- 11 Auken E, Christiansen AV, H.Westergaard J, Kirkegaard C, Foged N, Viezzoli A (2009) : An
12 integrated processing scheme for high-resolution airborne electromagnetic surveys, the SkyTEM
13 system. *Explor Geophys* 40(2):184–192. doi: <http://dx.doi.org/10.1071/EG08128>
- 14 Auken E, Christiansen AV, Kirkegaard C, Fiandaca G, Schamper C, Behroozmand AA, Binley A,
15 Nielsen E, Effersø F, Christensen NB, Sørensen K, Foged N, Vignoli G (2014) : An overview of
16 a highly versatile forward and stable inverse algorithm for airborne, ground-based and borehole
17 electromagnetic and electric data. *Explor Geophys* 46(3):223–235. doi: 10.1071/EG13097
- 18 Binley A, Hubbard SS, Huisman JA, Revil A, Robinson DA, Singha K, Slater LD (2015) : The
19 emergence of hydrogeophysics for improved understanding of subsurface processes over
20 multiple scales. *Water Resour Res* 51:3837–3866. doi: 10.1002/2015WR017016
- 21 Blaschek R, Hördt A, Kemna A (2008) : A new sensitivity-controlled focusing regularization scheme
22 for the inversion of induced polarization data based on the minimum gradient support.
23 *GEOPHYSICS* 73:F45–F54. doi: 10.1190/1.2824820
- 24 Carle SF (1999) T-PROGS: Transition Probability Geostatistical Software. Users Manual. Version
25 2.1. University of California, Davis
- 26 Carle SF, Fogg GE (1996) : Transition probability-based indicator geostatistics. *Math Geol* 28:453–
27 476. doi: 10.1007/BF02083656
- 28 Certes C, De Marsily G (1991) : Application of the pilot point method to the identification of aquifer
29 transmissivities. *Adv Water Resour* 14:284–300. doi: 10.1016/0309-1708(91)90040-U
- 30 Chen J, Hubbard S, Rubin Y (2001) : Estimating the hydraulic conductivity at the south oyster site
31 from geophysical tomographic data using Bayesian Techniques based on the normal linear
32 regression model. *Water Resour Res* 37:1603–1613. doi: 10.1029/2000WR900392
- 33 Christensen NK, Christensen S, Ferre TPA (2016) : Testing alternative uses of electromagnetic data to
34 reduce the prediction error of groundwater models. *Hydrol Earth Syst Sci* 20:1925–1946. doi:
35 10.5194/hess-20-1925-2016
- 36 Christiansen A V., Auken E, Sørensen K (2006) : The transient electromagnetic method. In: Kirsch R
37 (ed) *Groundwater Geophysics - A tool for hydrogeology*, first ed. Springer-Verlag,
38 Berlin/Heidelberg, pp 179–225
- 39 Clavier C, Coates G, Dumanoir J (1984) : Theoretical and Experimental Bases for the Dual-Water
40 Model for Interpretation of Shaly Sands. *Soc Pet Eng J* 24:153–168. doi: 10.2118/6859-PA



- 1 Constable SC, Parker RL, Constable CG (1987) : Occam's inversion: A practical algorithm for
2 generating smooth models from electromagnetic sounding data. *GEOPHYSICS* 52:289–300. doi:
3 10.1190/1.1442303
- 4 Cooley RL, Naff RL (1990) : Regression modeling of ground-water flow.
- 5 Day-Lewis FD (2005) : Applying petrophysical models to radar travel time and electrical resistivity
6 tomograms: Resolution-dependent limitations. *J Geophys Res* 110:B08206. doi:
7 10.1029/2004JB003569
- 8 Desbarats AJ, Srivastava RM (1991) : Geostatistical characterization of groundwater flow parameters
9 in a simulated aquifer. *Water Resour Res* 27:687–698. doi: 10.1029/90WR02705
- 10 Deutsch C V. (2006) : A sequential indicator simulation program for categorical variables with point
11 and block data: BlockSIS. *Comput Geosci* 32:1669–1681. doi: 10.1016/j.cageo.2006.03.005
- 12 Deutsch C V., Journel AG (1998) *GSLIB: Geostatistical Software Library and User's Guide*: Clayton
13 V. - Oxford University Press, Second Edi. Oxford University Press
- 14 Doherty J (2003) : Ground Water Model Calibration Using Pilot Points and Regularization. *Ground*
15 *Water* 41:170–177. doi: 10.1111/j.1745-6584.2003.tb02580.x
- 16 Doherty J (2010) *PEST, Model-Independent Parameter Estimation, User Manual*, 5th ed, 336 pp.,
17 Watermark Numerical Computing
- 18 Doherty J, Christensen S (2011) : Use of paired simple and complex models to reduce predictive bias
19 and quantify uncertainty. *Water Resour Res* 47(12):W12534. doi: 10.1029/2011WR010763
- 20 Doherty J, Welter D (2010) : A short exploration of structural noise. *Water Resour Res* 46
21 (5):W05525. doi: 10.1029/2009WR008377
- 22 Ferré T, Bentley L, Binley A, Linde N, Kemna A, Singha K, Holliger K, Huisman JA, Minsley B
23 (2009) : Critical Steps for the Continuing Advancement of Hydrogeophysics. *Eos, Trans Am*
24 *Geophys Union* 90:200. doi: 10.1029/2009EO230004
- 25 Fiandaca G, Kirkegaard C, Foged N, Christiansen AV, Auken E (2015) : Sharp Spatially-decoupled
26 Inversion of Airborne Electromagnetic Data for Improved Model Integration. In: *First European*
27 *Airborne Electromagnetics Conference*.
- 28 Fogg GE, LaBolle EM, Weissmann GS (1999) *Groundwater Vulnerability Assessment:*
29 *Hydrogeologic Perspective and Example from Salinas Valley, California*. American Geophysical
30 Union, Washington, D. C.
- 31 Gunnink JL, Siemon B (2015) : Applying airborne electromagnetics in 3D stochastic geohydrological
32 modelling for determining groundwater protection. *Near Surf Geophys* 13:45–60. doi:
33 10.3997/1873-0604.2014044
- 34 Harbaugh AW, Banta ER, Hill MC, McDonald MG (2000) *MODFLOW-2000, The U.S. Geological*
35 *Survey modular ground-water model: User guide to modularization concepts and the ground-*
36 *water flow process*. U.S. Geological Survey Open-File Report 00-92, 121 p.
- 37 He X, Koch J, Sonnenborg TO, Jørgensen F, Schamper C, Christian Refsgaard J (2014) : Transition
38 probability-based stochastic geological modeling using airborne geophysical data and borehole
39 data. *Water Resour Res* 50:3147–3169. doi: 10.1002/2013WR014593
- 40 Herckenrath D, Fiandaca G, Auken E, Bauer-Gottwein P (2013) : Sequential and joint



- 1 hydrogeophysical inversion using a field-scale groundwater model with ERT and TDEM data.
2 Hydrol Earth Syst Sci 17:4043–4060. doi: 10.5194/hess-17-4043-2013
- 3 Hyndman D., Tronicke J (2005) : Hydrogeophysical case studies at the local scale: the saturated zone.
4 In: Rubin Y, Hubbard SS (eds) Hydrogeophysics. Springer Netherlands, Dordrecht, pp 391–412
- 5 Jørgensen F, Lykke-Andersen H, Sandersen PBE, Auken E, Nørmark E (2003) : Geophysical
6 investigations of buried Quaternary valleys in Denmark: an integrated application of transient
7 electromagnetic soundings, reflection seismic surveys and exploratory drillings. J Appl Geophys
8 53:215–228.
- 9 Jørgensen F, Møller RR, Nebel L, Jensen N-P, Christiansen AV, Sandersen PBE (2013) : A method
10 for cognitive 3D geological voxel modelling of AEM data. Bull Eng Geol Environ 72:421–432.
11 doi: 10.1007/s10064-013-0487-2
- 12 Linde N, Finsterle S, Hubbard S (2006) : Inversion of tracer test data using tomographic constraints.
13 Water Resour Res. doi: 10.1029/2004WR003806
- 14 Marker PA, Foged N, He X, Christiansen A V., Refsgaard JC, Auken E, Bauer-Gottwein P (2015) :
15 Performance evaluation of groundwater model hydrostratigraphy from airborne electromagnetic
16 data and lithological borehole logs. Hydrol Earth Syst Sci 19:3875–3890. doi: 10.5194/hess-19-
17 3875-2015
- 18 Mazáč O, Kelly WE, Landa I (1985) : A hydrogeophysical model for relations between electrical and
19 hydraulic properties of aquifers. J Hydrol 79:1–19.
- 20 McNeill JD (1980) : Electromagnetic Terrain Conductivity Measurement at Low Induction Numbers,
21 Tech. Note TN-6.
- 22 Menke W (2012) Geophysical Data Analysis: Discrete Inverse Theory, Third Edition: MATLAB
23 Edition. Elsevier, Academic Press, Boston, USA.
- 24 Munday T, Gilfedder M, Taylor andrew r, Ibrahim T, Ley-cooper Y, Cahill K, Smith S, Costar A
25 (2015) : The role of airborne geophysics in facilitating long-term outback water solutions to
26 support mining in South Australia. Water - J Aust Water Assoc 42:138–141.
- 27 Oldenborger GA, Pugin AJ-M, Pullan SE (2013) : Airborne time-domain electromagnetics, electrical
28 resistivity and seismic reflection for regional three-dimensional mapping and characterization of
29 the Spiritwood Valley Aquifer, Manitoba, Canada. Near Surf Geophys 11:63–74. doi:
30 10.3997/1873-0604.2012023
- 31 Pollock DW (1994) User ' s Guide for MODPATH / MODPATH-PLOT , Version 3 : A particle
32 tracking post-processing package for MODFLOW , the U . S . Geological Survey finite-
33 difference ground-water flow model.
- 34 Portniaguine O, Zhdanov MS (1999) : Focusing geophysical inversion images. GEOPHYSICS
35 64:874–887. doi: 10.1190/1.1444596
- 36 Refsgaard JC, Christensen S, Sonnenborg TO, Seifert D, Højberg AL, Trolborg L (2012) : Review of
37 strategies for handling geological uncertainty in groundwater flow and transport modeling. Adv
38 Water Resour 36:36–50. doi: 10.1016/j.advwatres.2011.04.006
- 39 Revil A, Cathles LM (1999) : Permeability of shaly sands. Water Resour Res 35:651–662. doi:
40 10.1029/98WR02700
- 41 Revil A, Karaoulis M, Johnson T, Kemna A (2012) : Review: Some low-frequency electrical methods



- 1 for subsurface characterization and monitoring in hydrogeology. *Hydrogeol J* 20:617–658. doi:
2 10.1007/s10040-011-0819-x
- 3 Robinson DA, Binley A, Crook N, Day-Lewis FD, Ferré TPA, Grauch VJS, Knight R, Knoll M,
4 Lakshmi V, Miller R, Nyquist J, Pellerin L, Singha K, Slater L (2008) : Advancing process-based
5 watershed hydrological research using near-surface geophysics: a vision for, and review of,
6 electrical and magnetic geophysical methods. *Hydrol Process* 22:3604–3635. doi:
7 10.1002/hyp.6963
- 8 Schamper C, Jørgensen F, Auken E, Effersø F (2014) : Assessment of near-surface mapping
9 capabilities by airborne transient electromagnetic data — An extensive comparison to
10 conventional borehole data. *GEOPHYSICS* 79:B187–B199. doi: 10.1190/geo2013-0256.1
- 11 Seifert D, Sonnenborg TO, Refsgaard JC, Højberg AL, Troldborg L (2012) : Assessment of
12 hydrological model predictive ability given multiple conceptual geological models. *Water*
13 *Resour Res* 48:W06503. doi: 10.1029/2011WR011149
- 14 Siemon B, Christiansen AV, Auken E (2009) : A review of helicopter-borne electromagnetic methods
15 for groundwater exploration. *Near Surf Geophys* 7:629–646. doi: 10.3997/1873-0604.2009043
- 16 Slater L (2007) : Near Surface Electrical Characterization of Hydraulic Conductivity: From
17 Petrophysical Properties to Aquifer Geometries—A Review. *Surv Geophys* 28:169–197. doi:
18 10.1007/s10712-007-9022-y
- 19 Strebelle S (2002) : Conditional Simulation of Complex Geological Structures Using Multiple-Point
20 Statistics. *Math Geol* 34:1–21. doi: 10.1023/A:1014009426274
- 21 Sørensen KI, Auken E (2004) : SkyTEM – a new high-resolution helicopter transient electromagnetic
22 system. *Explor Geophys* 35:194–202.
- 23 Thomsen R, Søndergaard VH, Sørensen KI (2004) : Hydrogeological mapping as a basis for
24 establishing site-specific groundwater protection zones in Denmark. *Hydrogeol J* 12:550–562.
25 doi: 10.1007/s10040-004-0345-1
- 26 Viezzoli A, Christiansen AV, Auken E, Sørensen K (2008) : Quasi-3D modeling of airborne TEM
27 data by spatially constrained inversion. *GEOPHYSICS* 73:F105–F113. doi: 10.1190/1.2895521
- 28 Vignoli G, Fiandaca G, Christiansen AV, Kirkegaard C, Auken E (2015) : Sharp spatially constrained
29 inversion with applications to transient electromagnetic data. *Geophys Prospect* 63:243–255. doi:
30 10.1111/1365-2478.12185
- 31 Waxman MH, Smits LJM (1968) : Electrical Conductivities in Oil-Bearing Shaly Sands. *Soc Pet Eng*
32 *J* 8:107–122. doi: 10.2118/1863-A
- 33 Weissmann GS, Fogg GE (1999) : Multi-scale alluvial fan heterogeneity modeled with transition
34 probability geostatistics in a sequence stratigraphic framework. *J Hydrol* 226:48–65. doi:
35 10.1016/S0022-1694(99)00160-2
- 36 Zhou H, Gómez-Hernández JJ, Li L (2014) : Inverse methods in hydrogeology: Evolution and recent
37 trends. *Adv Water Resour* 63:22–37. doi: 10.1016/j.advwatres.2013.10.014

38

39



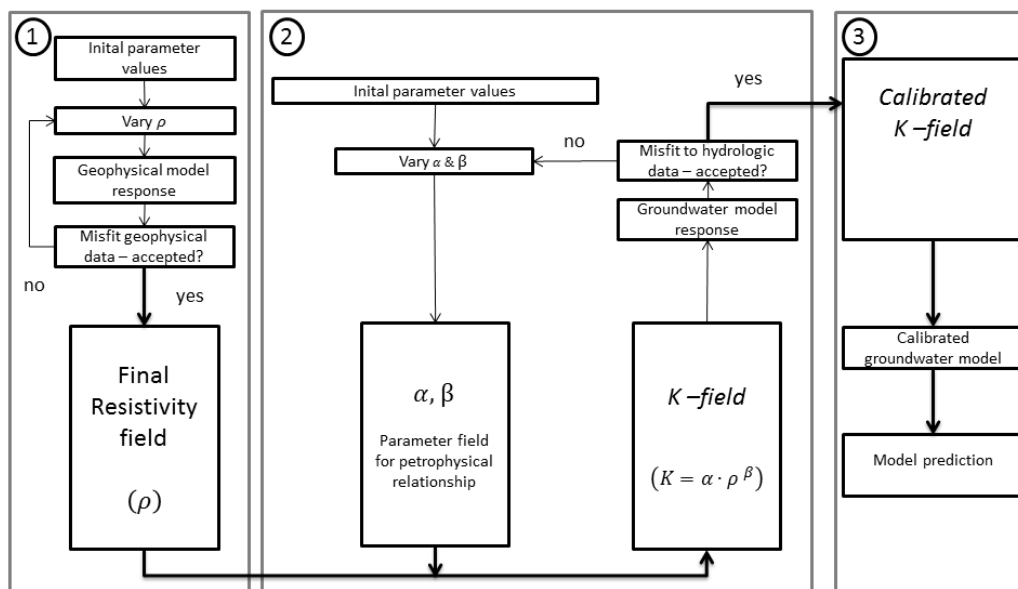
1 Table 1. Model structural accuracy comparison for groundwater model using both smooth or sharp
2 geophysical models and different background noise levels. The results are averaged over the 20
3 system realizations. A value of 1.0 means that the model's hydraulic conductivity field is in good
4 agreement with the reference field; a value of 0.0 means no agreement (see body text for exact
5 definition of "structural accuracy").

| | Layer 1 | Layer 2 | Layer 3 | Layer 4 | Layer 5 |
|-----------------|---------|---------|---------|---------|---------|
| SHI-1 Smooth | 0.89 | 0.79 | 0.56 | 0.54 | 0.64 |
| SHI-1 Sharp | 0.96 | 0.91 | 0.81 | 0.61 | 0.48 |
| SHI-3 Sharp | 0.96 | 0.92 | 0.82 | 0.64 | 0.5 |
| SHI-5 Sharp | 0.96 | 0.91 | 0.78 | 0.64 | 0.49 |
| SHI-10 Sharp | 0.96 | 0.9 | 0.78 | 0.6 | 0.46 |

6



1

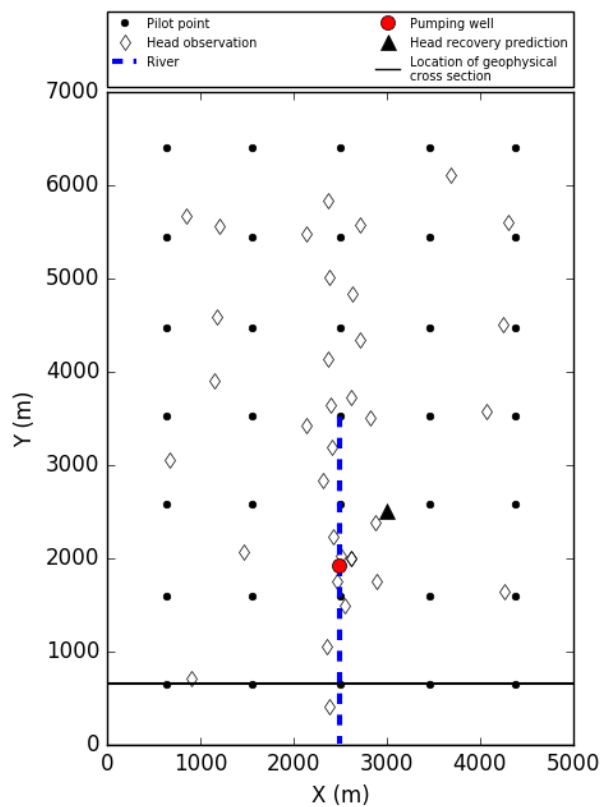


2

3 Figure 1. Conceptual flowchart for the sequential hydrogeophysical inversion. First step (box 1):
 4 geophysical inversion. Second step (box 2), groundwater model calibration where shape factors of the
 5 petrophysical relationship is estimated using hydrological data. Third step (box 3): The calibrated
 6 groundwater model is used for predictive modeling.

7

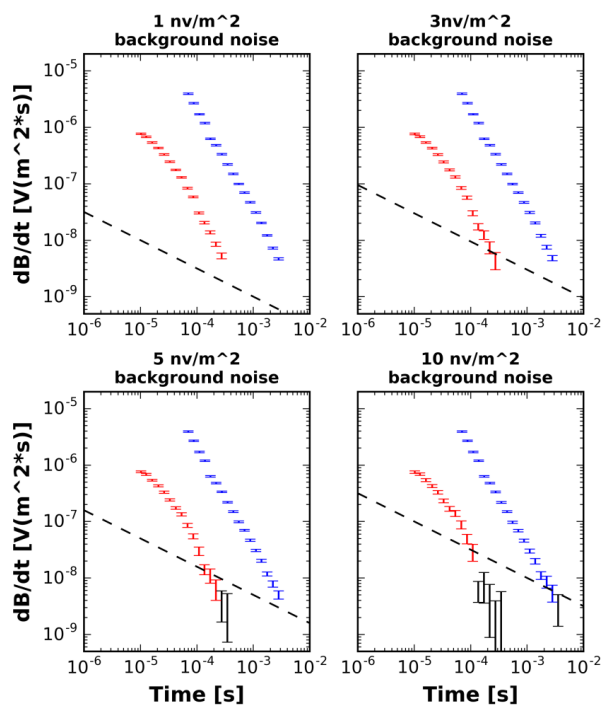
8



1

2 Figure 2. A map of locations of boreholes, a pumping well, pilot points, head recovery prediction and
3 location of a geophysical cross-section.

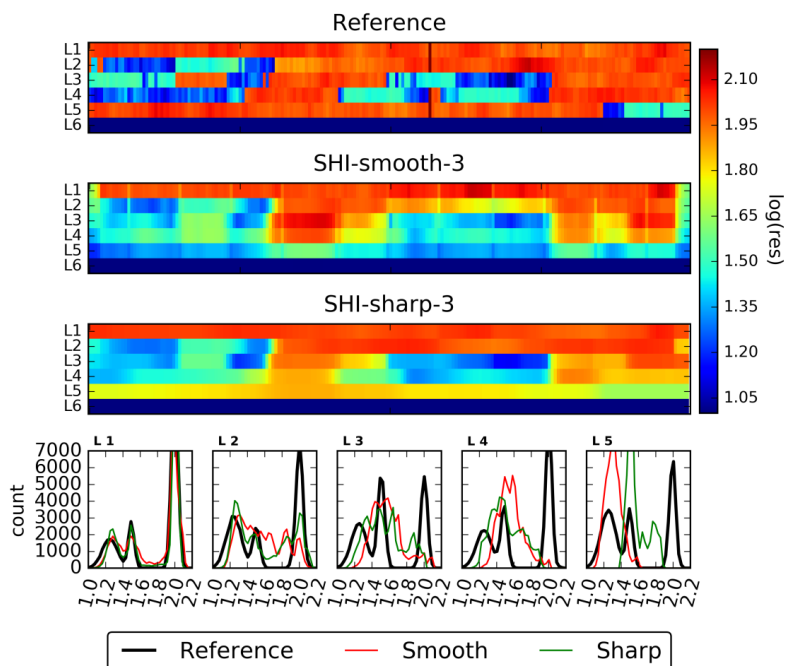
4



1

2 Figure 3. AEM sounding data corrupted by four levels of background noise. The black dashed curves
3 indicate the background noise levels, low and high moment earth responses are illustrated as red and
4 blue error bars, respectively, and the black error bars illustrate data which are removed by the data
5 processing

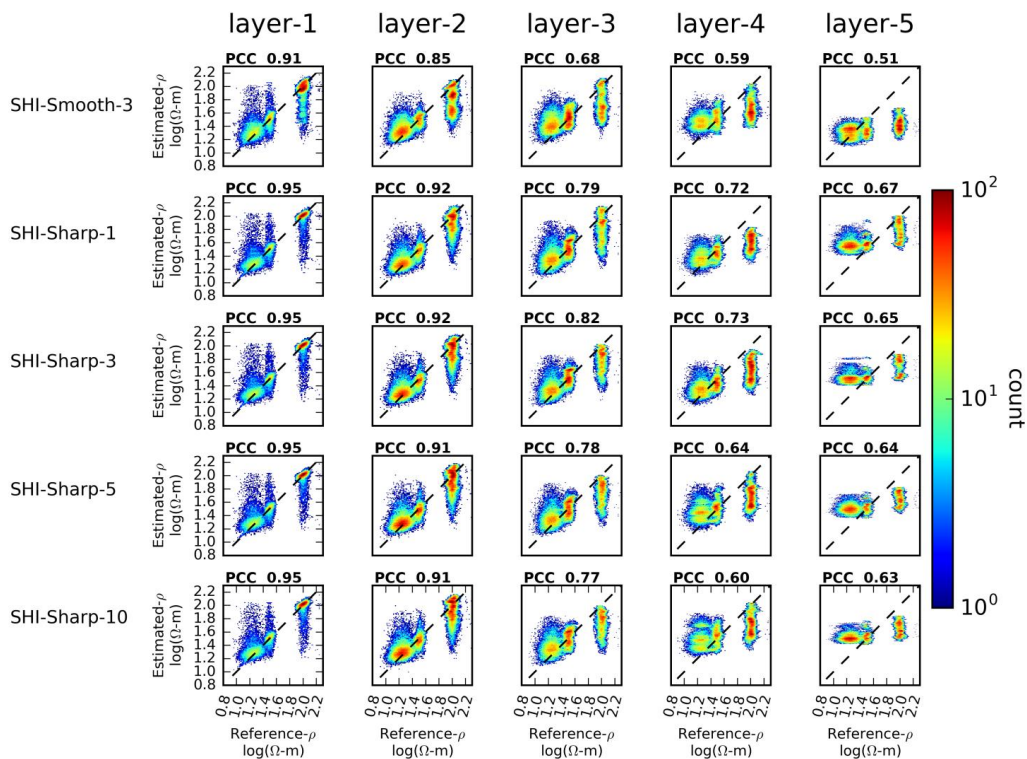
6



1

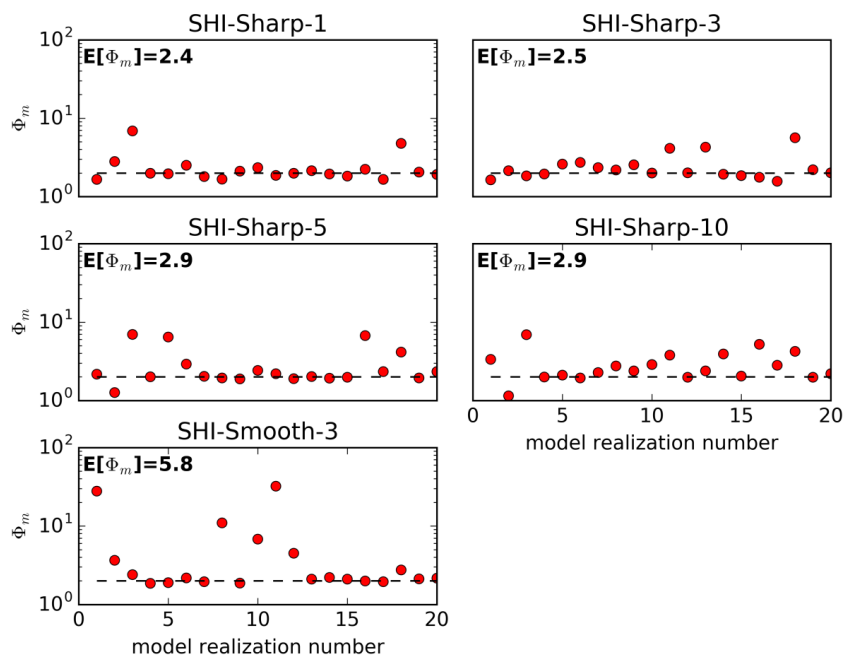
2 Figure 4. The figure shows an East-West cross section of resistivity for the reference system
 3 (realization number 20), and inversion results for Smooth and Sharp inversion, respectively. The last
 4 row shows at histogram of resistivity for each layer. The black curve is the resistivity distribution for
 5 the reference system, the red curve shows the resistivity distribution for the smooth inversion, and
 6 finally the green curve shows the resistivity distribution for the smooth inversion.

7



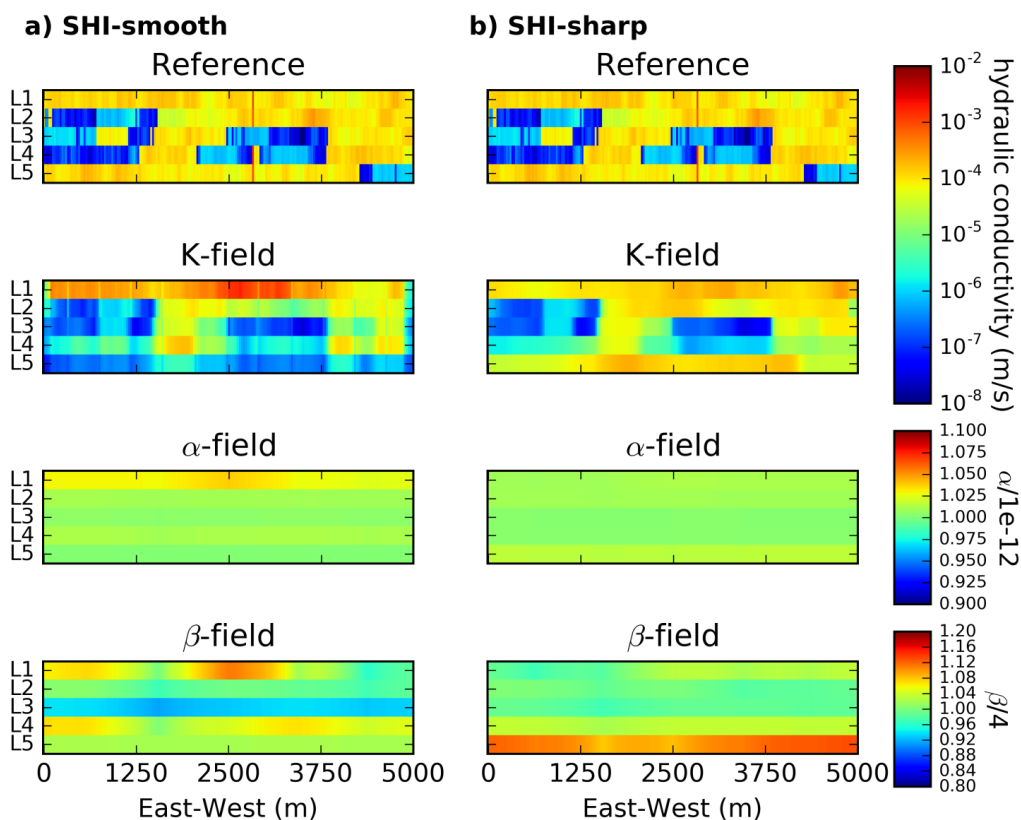
1

2 Figure 5. Scatterplot of true and estimated electrical resistivity field for smooth geophysical inversion
 3 and sharp geophysical inversion for different data quality of the AEM data for model realization
 4 number 20. On top of each window is Pearson correlation coefficient (PCC) calculated.



1

2 Figure 6. Measurement objective function value obtained for the various groundwater model
3 calibration cases, while $E[\Phi_m]$ is the mean value across all 20 different system realizations. The
4 dashed line indicates the expected target value for the model calibrations.



1

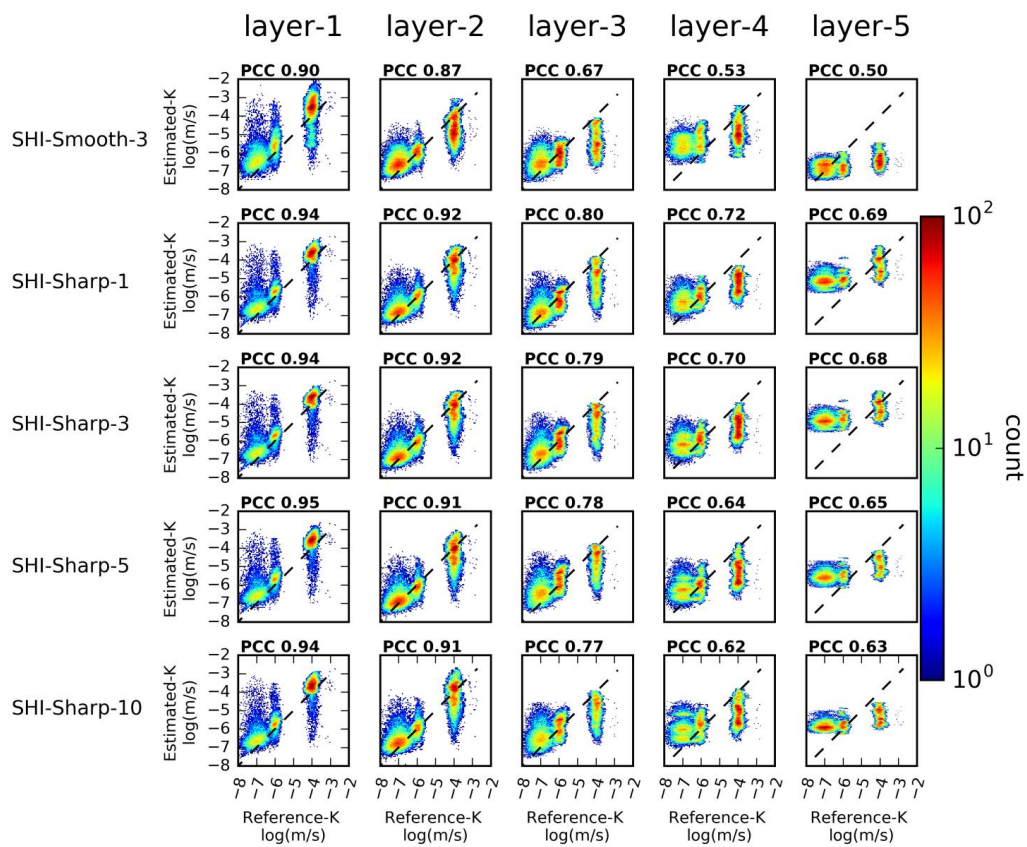
2 Figure 7. East-West cross-section for model realization number 20. a) shows the parameters fields for
 3 the SHI-smooth calibrated model. b) Shows the parameters fields for the SHI-sharp calibrated model.

4 First row shows the reference K-field, second row shows the estimated K-field, third and fourth row
 5 shows shape factors of the petrophysical relationship for alfa and beta, respectively.

6

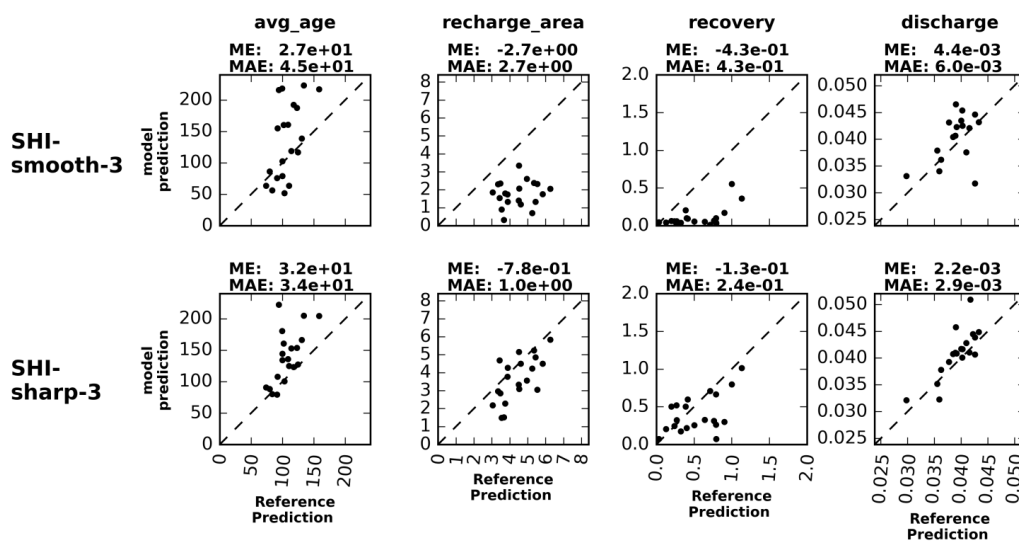
7

8

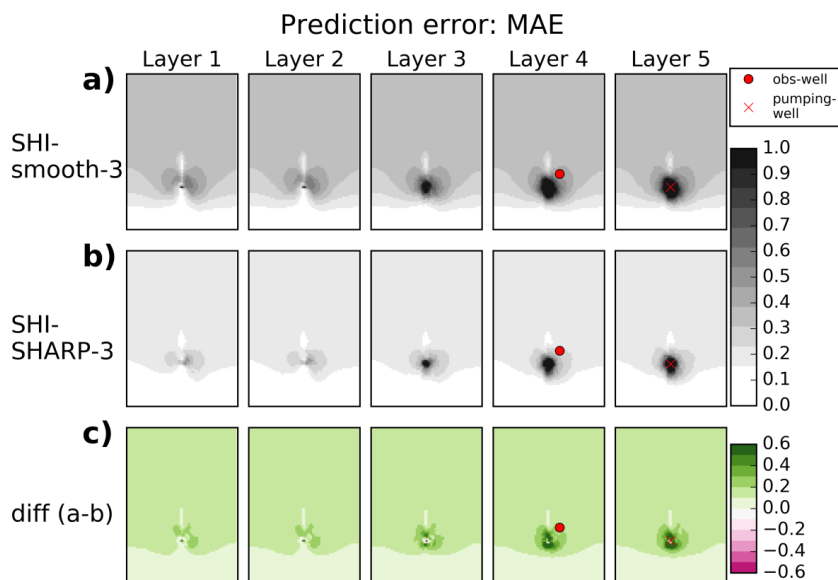


1

2 Figure 8. Scatterplot of true and estimated hydraulic conductivity field for smooth geophysical
 3 inversion and sharp geophysical inversion for different data quality of the AEM data for model
 4 realization number 20. On top of each window is Pearson correlation coefficient (PCC) calculated.



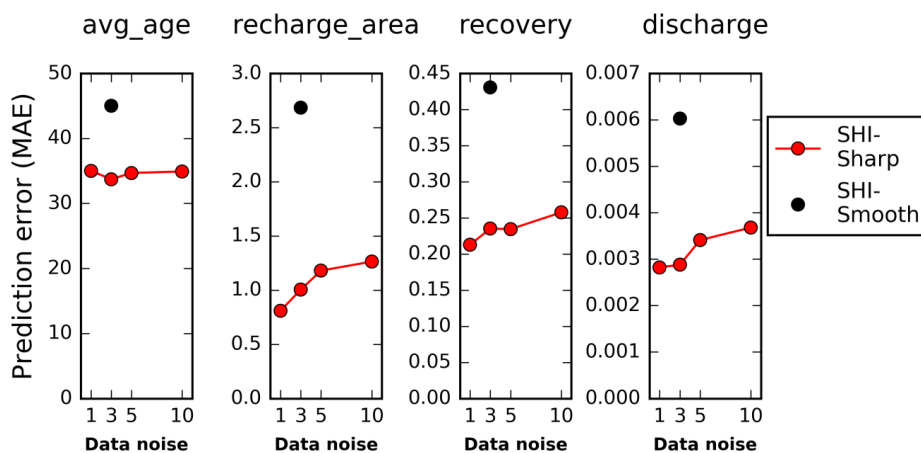
1
 2 Figure 9. Scatter plots of calibrated model prediction versus the reference model prediction using
 3 results from the 20 system realizations. The plots in the first column is for head, the second column is
 4 for head recovery when pumping has stopped, third column is groundwater discharge to the river after
 5 pumping has stopped, fourth and fifth column is the average age and recharge area to the pumping
 6 well. *ME* and *MAE* are used to quantify the prediction error on basis of the 20 realizations.



1

2 Figure 10. MAE contour map for head recovery prediction. a) For predictions using the SHI-smooth
3 models. b) For predictions using the SHI-smooth models. c) Difference between maps shown in a)
4 and b). Red dot marks the location of the observation well for the head recovery prediction shown in
5 Figure 9. The red cross marks the location of the pumping well.

6



1

2 Figure 11. Prediction error as function of the background noise on the geophysical data. The black dot
3 is the SHI-smooth models using a background noise level of 3nV/m^2 . The red dots are the SHI-sharp
4 models as a function of background noise level.